Energy Storage Materials 73 (2024) 103842

Contents lists available at ScienceDirect

Energy Storage Materials

journal homepage: www.elsevier.com/locate/ensm

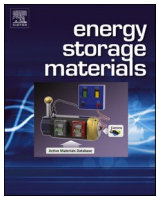

Probing degradation at solid-state battery interfaces using machine-learning interatomic potential

Kwangnam Kim [a,*], Nicole Adelstein [a,b], Aniruddha Dive [a], Andrew Grieder [a,b,c], ShinYoung Kang [a], Brandon C. Wood [a,*], Liwen F. Wan [a,*]

[a] Laboratory for Energy Applications for the Future (LEAF), Lawrence Livermore National Laboratory, Livermore, CA 94550-9234, United States
[b] Department of Chemistry and Biochemistry, San Francisco State University, San Francisco, CA 94132-1740, United States
[c] Department of Chemistry and Biochemistry, University of California, Santa Cruz, CA 95064-1099, United States

ARTICLE INFO

Keywords:
Machine learning interatomic potential
Solid state batteries
Interfacial degradation
Ion transport
Atomistic modeling

ABSTRACT

Solid-state batteries featuring fast ion-conducting solid electrolytes are promising next-generation energy storage technologies, yet challenges remain for practical deployment due to electro-chemo-mechanical instabilities at solid-solid interfaces. These interfaces, which include homogeneous/internal interfaces such as grain boundaries (GBs) and heterogeneous/external interfaces between solid-electrolyte and electrode materials, can impede Li-ion transport, deteriorate performance, and eventually lead to cell failure. Here we leverage large-scale molecular simulations, enabled by validated machine-learning interatomic potentials, to directly probe the onset of interfacial degradation at the garnet $Li_7La_3Zr_2O_{12}$ (LLZO) solid-electrolyte/$LiCoO_2$ (LCO) cathode interface. By surveying different interfacial geometries and compositions, it is found that Li-deficient interfaces can lead to severe interfacial disordering with cation mixing and Co interdiffusion from LCO into LLZO. By contrast, Li-sufficient interfaces are less disordered, although elemental segregation with local ordering is observed. As a consequence of Co interdiffusion, Co-rich regions are formed at the GBs of LLZO due to cation segregation and trapping effects. This behavior is independent of the GB tilting axis, degree of disorder at the GBs, and Co concentration, which implies Co clustering at GBs is a general phenomenon in polycrystalline LLZO and can dictate its overall transport and mechanical properties. Our findings elucidate the underlying fundamental mechanisms that give rise to experimentally observed physicochemical properties and provide guidelines for interface design that can mitigate interfacial degradation and improve cycling performance.

1. Introduction

As a promising future energy storage solution, solid-state battery (SSB) technologies with less flammable and non-volatile solid electrolytes (SEs) have attracted great attention in recent decades for their potential to achieve higher energy densities and improved safety compared to conventional Li-ion batteries [1-6]. One promising SE material is the garnet-type oxide $Li_7La_3Zr_2O_{12}$ (LLZO), which exhibits a relatively high ionic conductivity (10^{-3} – 10^{-4} S/cm), a wide electrochemical window, and a good stability with Li metal [7-10]. Nevertheless, challenges remain to employ LLZO SE in practical SSBs due to undesired side reactions occurring at both homogenous/internal interfaces (i.e., grain boundaries; GBs) and heterogenous/external interfaces with electrodes.

Internally, Li dendrite growth along GBs can result in short circuiting [11], and GB segregation of dopants can lead to the formation of highly resistant secondary phases [12-14]. Externally, overall cell performance can be dictated by electro-chemo-mechanical instabilities at interfaces between LLZO and cathode active materials, e.g., $LiCoO_2$ (LCO) and $LiNi_xMn_yCo_{1-x-y}O_2$ (NMC). For example, the volume variation experienced by the cathode particles during cycling can lead to mechanical failure and capacity fade due to contact loss at the interfaces from delamination and/or cracking, [15-19]. In addition, although less severe than sulfide-based SEs, LLZO is not (electro)chemically stable against common cathode materials [20,21] especially during high-temperature co-sintering. For example, La-M-O secondary phases, where M refers to one or more transition metals, have been identified at LLZO|cathode interfaces due to initial interfacial degradation during preparation [22, 23]. The transition metals, such as Co from LCO, can interdiffuse into the SE, leading to the formation of secondary phases within bulk SE with

* Corresponding author.
E-mail addresses: kim109@llnl.gov (K. Kim), wood37@llnl.gov (B.C. Wood), wan6@llnl.gov (L.F. Wan).

https://doi.org/10.1016/j.ensm.2024.103842
Received 31 December 2023; Received in revised form 14 June 2024; Accepted 14 October 2024
Available online 16 October 2024

high ionic resistance [24,25]. To better address these interfacial issues and establish mitigation strategies, it is imperative to obtain a fundamental, atomic-level understanding of the key physicochemical phenomena at LLZO|cathode interfaces. However, directly probing these dynamically evolving interfaces and thus resolving the underlying atomic features that lead to initial degradation remains very challenging [26]. Experimentally, extraordinary spatial and temporal resolution is required, whereas computationally, simulations must span the extended time and length scales associated with the interfacial degradation process.

Recently, machine-learning (ML) interatomic potentials have emerged as a promising avenue to perform large-scale atomic simulations with quantum-level accuracy by training ML models with ab-initio simulation data [27]. They have been successfully applied to study GBs of various systems [28-32], as well as interfacial interactions of molecules[33-39] and nanoparticles[40,41] on solid surfaces [42,43]. In addition, a few studies have applied ML potentials to examine phenomena at solid-solid interfaces, such as disordering and nucleation of NiSi at a Ni-Si interface [44], Li transport at ordered interfaces between Li metal and decomposed Li_6PS_5Cl SE phases including Li_2S, Li_3P, and LiCl [45], and formation of polysulfides and S clusters at the S_8/Li_3PS_4 interfaces in Li-S batteries [46]. These and other recent advancements in developing and applying ML models encourage their use as powerful tools to also understand interfacial degradation in energy storage devices [47-50].

In this work, we developed an ML interatomic potential to directly explore non-equilibrium evolution and degradation at complex interfaces between LLZO SEs and LCO cathodes at the atomistic scale. The developed ML model can accurately predict the structural, vibrational, and dynamical properties of disordered LLZO|LCO interfaces (as well as bulk phases of LLZO and LCO) with quantum-level accuracy. Our simulations survey various distinct LLZO|LCO interfaces to reveal that Li concentration at the interface is a key factor that governs interfacial stability and cation reordering. We further observe that disordering and cation mixing at interfaces can lead to long-range interdiffusion of Co ions from LCO into LLZO, although this does not significantly affect Li transport in bulk crystalline LLZO. However, the interdiffused Co tends to segregate at disordered GBs of LLZO, forming Co clusters that can lead to prenucleation of Co-rich secondary phases at LLZO GBs. Our insights into the structure-property relationships associated with chemical degradation and ion transport at complex oxide interfaces allude to possible interface designs that can minimize interfacial degradation and improve the cycling performance of SSBs.

2. Methods

The ML interatomic potential was developed based on the neural network (NN) approach implemented in the *n2p2* code [51,52]. The NN model comprised two hidden layers each with 20 neurons, and the local atomic environment of input features was described using the radial and angular symmetry functions suggested by Behler and Parrinello with a 6 Å cutoff radius [32,53]. The training data, consisting of atomic structures with their corresponding energies and forces, was collected from ab-initio molecular dynamics (AIMD) simulations performed at a wide range of temperatures and compositions. (See "Machine-learning Model" and "Ab-initio Simulations and Structure Data" sections in the Supporting Information (SI) for details of the ML model and data structure.)

The dataset contained a total of 12,651 structures of LLZO, LCO, LLZO|LCO mixtures, and Co-doped amorphous LLZO. These data represent individual materials as well as disordered local atomic environment at interfaces. The LLZO and LCO data included crystalline and amorphous structures generated from AIMD at 1000 – 2000 K and 4000 K, respectively. The LLZO|LCO mixture models with five different compositions (Table S1) are proxies for local atomic environments at interfaces with a wide range of Li concentrations (i.e., Li deficient/sufficient conditions) and stoichiometric variations of other cations. The Co-doped LLZO data were obtained by replacing Li, La, or Zr with Co in an amorphous LLZO unit cell at six different doping concentrations, which was intended to capture the possible dynamical evolution of Co atoms in LLZO from diffusion or segregation. (See Table S2 for a listing of the number of structures for each data type.) This approach to generate training data for disordered/reactive solid-solid interfaces can be generalized since it enables to include necessary information of diverse local compositions and atomic configurations at interfaces, as emphasized in literature regarding the needs of data at interface regions [42].

Randomly selected from the entire dataset, ten percent was used for testing (i.e., test dataset) and not involved in weight updates during training. The training root mean squared errors (RMSEs) of our developed ML model are 7.54 meV/atom and 0.348 eV/Å for energies and forces, respectively. To test the performance, we further performed molecular dynamics simulations using the ML model (MLMD) within the nvt ensemble at 2000 K for 100 ps for all atomic systems included in the dataset (details of MLMD simulations are provided in the "Simulation Methods with ML potential" section in the SI). Figure S1 compares the total energies and atomic forces predicted from the ML model and computed from DFT for atomic structures collected at every 1 ps (i.e., snapshots) from MLMD, demonstrating successful reproduction of DFT results from the developed ML model.

Table 1 summarizes the RMSEs of energies and forces, and their R^2 values are shown in Figure S1 (R^2 measures the similarity between prediction and observation [54]; see ref. [32] for the evaluation method). The R^2 values for each system were > 0.89 and > 0.96 for energies and forces, respectively, further confirming that our ML model can predict energy and force values close to those of DFT. The RMSEs of forces are < 0.3 eV/Å for all systems, and the RMSEs of energies range from 4.3 to 28.6 meV/atom. The RMSEs are low considering extreme complexity of reactive interfaces of interest in this study with two solid materials having three or more elements in each material and random mixing between these materials with five elements in total at high temperatures up to 2000 K; indeed, the RMSEs are similar to those from a ML model reported for F-Pd|CeO_2 (23 meV/atom and 0.23 eV/Å) and F-Pd|SiO_2 (12 meV/arom and 0.33 eV/Å) interfaces with four elements at 800 K [55], implying a superior performance of our ML potential.

Table 1
Energy (meV/atom) and force (eV/Å) errors of snapshots from MLMD simulations at 2000 K versus DFT. "Unseen" indicates that the ML model did not learn the systems. For Co-doped LLZO, $n\mathrm{Co}_{x=\mathrm{Li,\ La,\ or\ Zr}}$ indicates species x replaced by n Co atom(s) in a unit cell. Values in parenthesis are R^2 (see Figures S1, S5, and S10 for detailed data).

System type		Energy	Force
LLZO	Cubic	4.3 (0.99)	0.14 (0.99)
	Amorphous	11.0 (0.97)	0.19 (0.98)
LCO	Layered	8.0 (0.99)	0.19 (0.99)
LLZO-LCO mixtures	Model #1	21.9 (0.93)	0.26 (0.96)
	Model #2	22.4 (0.90)	0.28 (0.96)
	Model #3	24.9 (0.91)	0.27 (0.96)
	Model #4	28.6 (0.96)	0.28 (0.96)
	Model #5	23.9 (0.93)	0.29 (0.96)
Co-doped amorphous LLZO	$6\mathrm{Co}_{\mathrm{Li}}$	27.6 (0.89)	0.28 (0.96)
	$6\mathrm{Co}_{\mathrm{La}}$	15.6 (0.96)	0.22 (0.97)
	$6\mathrm{Co}_{\mathrm{Zr}}$	20.3 (0.95)	0.24 (0.97)
LLZO-LCO mixtures (unseen)	Model #1	15.8 (0.93)	0.27 (0.96)
	Model #2	20.9 (0.92)	0.26 (0.96)
	Model #3	26.2 (0.95)	0.26 (0.96)
	Model #4	25.8 (0.94)	0.27 (0.96)
	Model #5	22.6 (0.96)	0.28 (0.96)
LLZO-LCO interfaces	LLZO(001)/LCO (104)	17.9 (0.97)	0.26 (0.97)
	LLZO(001)/LCO (100)	15.5 (0.99)	0.27 (0.96)
	LLZO(001)/LCO (110)	15.6 (0.96)	0.27 (0.96)

The RMSEs in energies mostly arise from a constant shift of the ML-predicted energies compared to DFT (Figure S1). The consistent shift is likely due to the bias term for the output node in the NN models, which is optimized to minimize the energy errors for training data and does not affect the force prediction since the bias term is independent of NN inputs. The shift would be larger for ML models with higher complexity covering various compositions and materials, e.g., disordered interfaces in this study. Thus, the shift does not affect the ability of the ML model to perform high-fidelity dynamic simulations since the NN model remains aware of the DFT energy-structure relation with accurate force predictions, as shown by the high R^2 values. Note that our ML model did not learn and do not predict electron information, though it would capture oxidation states of Co implicitly since different oxidation states lead to different local atomic environment.

Next, we compared the predicted radial distribution functions (RDFs), vibrational spectra, and Li diffusivities of the atomic systems in the training dataset to those obtained from AIMD at 2000 K (see "Analysis Methods" section in the SI for details of property calculations). Figure S2 shows that the ML model predicts accurate RDFs, with peak and valley positions similar to those obtained from AIMD. The ML-calculated elemental-decomposed vibrational spectra and mean-squared displacements (MSDs) of Li atoms in all systems are also close to those derived from AIMD (Figures S3 and S4). Moreover, we tested five additional LLZO|LCO mixtures with various stoichiometries (Table S3) that the ML model had not learned, i.e. "unseen" systems. The energy and force errors show R^2 values > 0.92 and > 0.96, respectively (Table 1 and Figure S5). Fig. 1 demonstrates accurate ML model predictions of the RDFs, elemental vibrational spectra, and Li MSDs of unseen mixture model #1 (see Figures S5–8 for validation results of other unseen mixture models). We quantified the errors in RDFs, vibrational spectra, and MSDs by using the positions of the first peaks in RDFs, the positions in the highest peaks in vibrational spectra, and the diffusivities compared to AIMD simulations, as shown in Figures S2-S4 and Figures S6-S8. Throughout all test cases, the RMSE is 0.054 Å for RDFs and 16.4 cm^{-1} for vibration spectra, respectively, and the average error in diffusivities is 16.9 %, implying a superior performance of our ML model. These results signify that our developed ML model can accurately simulate the structural and dynamic behavior of atomic species at LLZO|LCO interfaces with distinct local atomic environments.

It is noteworthy to mention that the developed ML model can perform simulations for tetragonal LLZO even tetragonal structure data were not included in the dataset. The RMSEs in energies and forces for tetragonal LLZO structures obtained from MLMD with npt ensemble at 700 K are very low, only 5.2 meV/atom and 0.09 eV/Å with 0.99 R^2 values for both energy and force (Figure S9a). Also, the predicted tetragonal-cubic transition temperature by MLFF is between 850 – 900 K (Figure S9b), very close to an experimental measurement of 918 K [56]. It seems to be enabled by including amorphous LLZO structure data that provides diverse atomic environments covering structural characteristics in tetragonal LLZO. The results indicate the ability of our ML potential for simulations including the phase transition that may occur at the interfaces between LLZO and LCO [25].

For further verification, we performed MLMD simulations for three LLZO|LCO interfaces between the cubic LLZO (001) plane and nonpolar LCO (104), (100), and (110) planes [57] for 1 ns at 2000 K (system sizes were 744, 432, and 480 atoms, respectively). Idealized interfaces were initially prepared without atomic disordering. The force RMSEs for MD snapshots obtained every 10 ps were smaller than 0.27 eV/Å, with R^2 values larger than 0.96. The energy errors were also small, with R^2 values > 0.96 (Table 1 and Figure S10). Again, the energies calculated by DFT and the ML model are linearly correlated, implying that the ML model is able to capture the underlying structure-energy relation. More importantly, the errors remain considerably small even at amorphized or partially decomposed LLZO|LCO interfaces (Figure S11), implying that the ML model can perform reliable simulations of interfacial evolution. We note that the ML model predicts interdiffusion of Co, La, and Zr cations across the interfaces similarly to AIMD, as illustrated in our simulation of the LLZO(001)|LCO(100) interface (Figure S11). In summary, these test results verify that our ML model can perform atomic simulations to study the dynamical evolution of complex LLZO|LCO interfaces with quantum-level accuracy.

3. Results and discussion

3.1. Chemical degradation of LLZO|LCO interfaces

To investigate the initial stage of interfacial degradation, we performed MLMD simulations of four distinct LLZO|LCO interfaces: an LLZO (001) facet interfacing with three nonpolar LCO (104), (100), and (110) surfaces and one polar LCO (003) surface. The system sizes were chosen to be large enough to probe the structural evolution of disordered interfaces; edge lengths of the simulation cells were at least 51.5 Å with $> 17{,}000$ atoms, which ensured residual lattice mismatches at the interfaces were smaller than 2.5 % (see Figure S12 and Table S4 for details of the interface models). Taking advantage of the periodic boundary conditions, we simultaneously modeled two chemically distinct interfaces normal to the LLZO|LCO boundaries: Li-deficient interfaces, which mimic the Li loss condition in LLZO during high-temperature sintering [58]; and Li-sufficient interfaces.

Fig. 2a shows a snapshot of the LLZO(001)|LCO(104) interface after 10 ns MLMD simulation at 1500 K. The Li-deficient interface undergoes significant disordering through intermixing of LLZO and LCO. Co ions

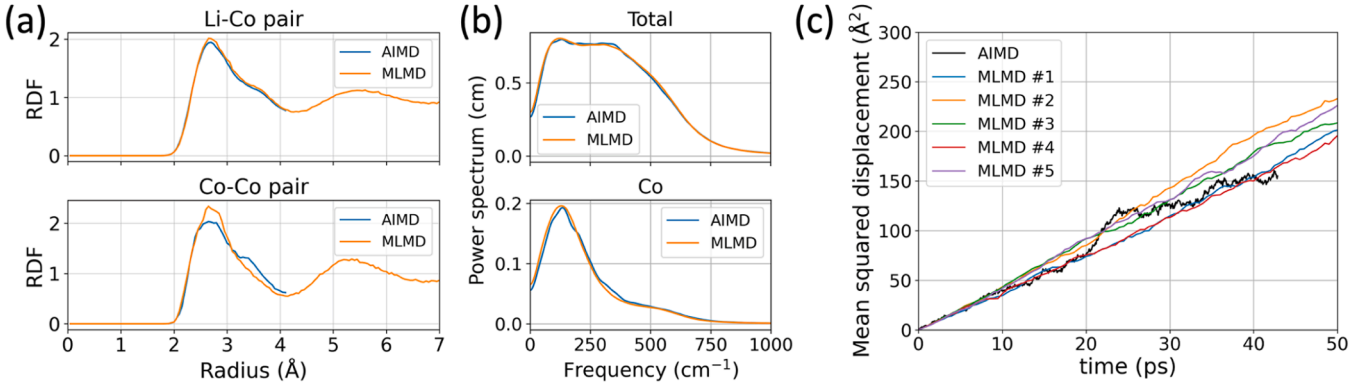

Fig. 1. Performance test for the unseen LLZO|LCO mixture model #1 by comparing AIMD and MD with the ML potential (MLMD) at 2000 K: (a) radial distribution functions (RDFs) of Li-Co and Co-Co pairs (see Figure S6a for other pairs), (b) total and element-resolved vibrational power spectra (see Figure S7a for other elements), and (c) mean squared displacements of Li atoms (five MLMD simulations). AIMD simulations were performed for 40 ps production time using a single unit cell and MLMD were performed for 100 ps using a 2 × 2 × 2 supercell (nvt ensemble).

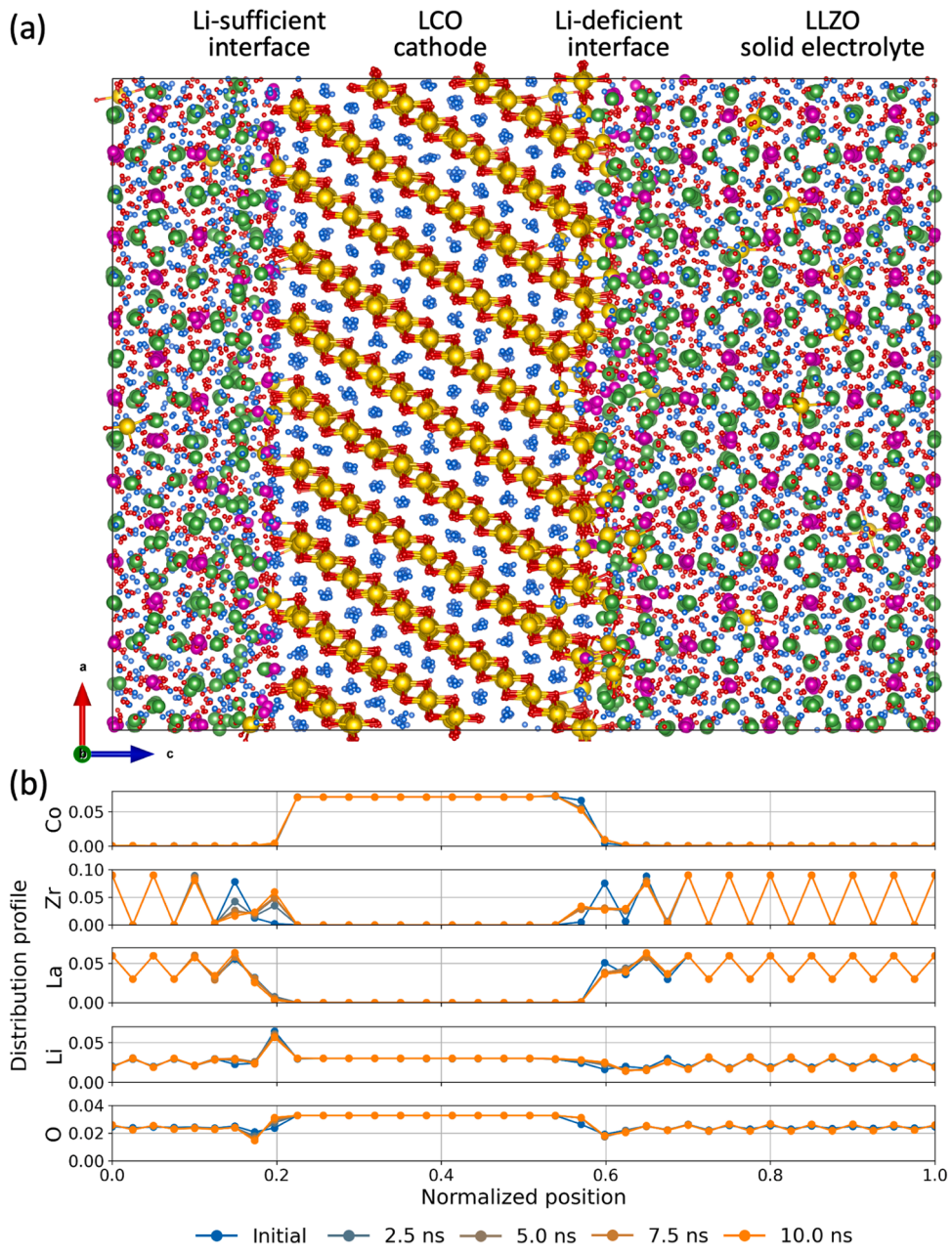

Fig. 2. (a) LLZO(001)|LCO(104) interface model after a 10 ns MLMD simulation at 1500 K (the initial configuration is shown in Figure S12). Yellow spheres represent Co ions, La is green, Zr is magenta, Li is blue, and O is red. Li-sufficient and Li-deficient conditions are represented at the left and right interfaces, respectively, which result in different interfacial evolution propensities. (b) Distribution profiles of elements as a function of position normal to interface plane (i.e., *c* direction) at different simulation times.

slip away from LCO and diffuse into the disordered LLZO, while La and Zr ions invade the surface layer of LCO. Fig. 2b quantifies the evolving degree of cation intermixing and shows that the concentration of Co ions decreases at the LCO surface layer and the distributions of La and Zr ions become flat at the interface. Interestingly, we observe long-range interdiffusion of Co ions into cubic LLZO, as evidenced by the finite Co distribution in the central region of LLZO at the later simulation stages. This finding agrees well with previous experiments, in which Co penetration into bulk LLZO was observed after high-temperature co-sintering of LLZO and LCO [24,25]. Since no La and Zr-related defects were found in LLZO, we presume that Co ion diffusion in bulk LLZO follows Li migration pathways, similar to the speculation of Din et al. that the color change in Co-doped LLZO may be related to Co ions residing at tetrahedral sites [25]. Details of the Co migration mechanism within bulk cubic LLZO will be discussed in the following subsections.

In contrast, the Li-sufficient interface shows less disordering than the Li-deficient interface (Fig. 2a). There is no significant intermixing of Co ions at the interface, although strong segregation of Zr and O ions near the LCO surface is observed as shown in Fig. 2b. Concurrent motion of Zr and O ions is likely favored to maintain charge balance, and as a result, Li and Zr cations and O anions are locally ordered alternatingly from the LCO surface and form an additional layer with the same configuration to the LCO (104) facet. Based on this observation, we speculate that secondary oxide phases may be formed at the Li-sufficient interfaces due to cation segregation, which can effectively block Co interdiffusion. In addition, we observe a separation between La and Zr ions that results in a La-dominant layer underneath the Li-Zr layer formed right at the interface, indicating the initial buildup of a space charge layer.

Similar to the LLZO(001)|LCO(104) interface, other interfaces with LCO (100) and (110) planes also experience strong disordering, cation intermixing, and long-range migration of Co ions into LLZO under Li-deficient conditions (Figures S13a and S14a). Under Li-sufficient conditions, Zr ions again segregate to the LCO surface, and some of them reside at Co sites adjacent to the LCO surface, showing a similar local ZrO_6 arrangement as in LCO. The concentration of La at the Li-sufficient LCO(100) interface does not change, implying a separation between La and Zr and the formation of a La-dominant layer similar to the Li-sufficient LCO(104) interface (Figure S13b). However, La ions are found to segregate to the LCO surface at the Li-sufficient LCO(110) interface (Figure S14b). These results indicate various degree of interfacial degradation propensities depending on the crystallographic orientations of LCO and its surface chemistry, although the qualitative distinctions between the Li-sufficient and Li-deficient interfaces are retained.

An interesting exception is the LLZO(001)|LCO(003) interface, which shows a different behavior from other interfaces due to special configurations of LCO layers parallel to the interfacial plane (Figure S15a). At the Li-deficient interface, a stable CoO_2 surface layer with a complete CoO_6 octahedral sub-structure effectively prevents Co ions from interdiffusion. Only the LLZO surface undergoes disordering, with Li ions segregating towards the LLZO|LCO interfaces, as shown by the increased Li concentration in Figure S15b. This reordering seems to form an additional layer with the same configuration as the Li-only layer of the LCO (001) facet. Under Li-sufficient conditions, Zr-ion segregation shows similar behavior at the LLZO(001)|LCO(003) interface as for other interfaces. Figure S15b reveals that the Zr concentration increases towards the LCO surface while the Li density decreases at the LCO surface with no change in the La profile, indicating the formation of a La-dominant layer at the Li-sufficient interface. In general, our results suggest that Zr segregation is a common phenomenon at the Li-sufficient interfaces.

We note here that during the course of 10 ns of MLMD simulations, three Co ions were found to diffuse into LLZO at the Li-deficient LCO (003) interface, forming Co vacancies in the CoO_2 surface layer (Figures S15 and S16). These vacancies were subsequently filled with Li ions, likely due to their small sizes. To evaluate the kinetics across LCO (003) plane, we calculated the migration barrier of Li ion at Co vacancy on the outer-most LCO(003) surface at the interface hopping into a Li vacancy in the inner Li layer by the nudged elastic band (NEB) method [59] with the MLFF model and an interface snapshot from MLMD after 10 ns (Fig. 3). We found that the migration barrier is 0.88 eV for lithiation and 0.39 eV for delithiation direction (reverse direction) at the fully lithiated state, which is higher than the barrier for Li migration along the Li layer in bulk LCO (about 0.3 eV) but can decrease at partially lithiated states [60]. This observation suggests a novel mechanism of Li transport across LCO layers via Co vacancies formed during co-sintering at high temperatures with LLZO and implies that LLZO (001)|LCO(003) interfaces may not completely block Li intercalation.

In summary, direct observation of the structural and chemical evolution at the LLZO|LCO interfaces at the atomic scale using our ML interatomic potential elucidates how the surface chemistry of LLZO and LCO affect the stability of the LLZO|LCO interface and its preferred local configurations that dictate Li-ion transport behavior. By surveying various LLZO|LCO interfaces with different crystallographic orientations and initial Li concentrations, we can generally infer severe cation interdiffusion at Li-deficient interfaces and Zr segregation at Li-sufficient interfaces. More specifically, large disordering and cation intermixing at the Li-deficient interfaces can lead to long-range interdiffusion of Co ions into LLZO. These results highlight the importance of preventing Li loss during high-temperature co-sintering of LLZO|LCO interfaces to alleviate interfacial degradation.

3.2. Ion transport in Co-doped cubic LLZO

Our MLMD simulations reveal interdiffusion of Co ions across the LLZO|LCO interfaces during initial interfacial degradation, followed by long-range diffusion of Co ions into bulk LLZO. However, the performance implications of these processes are determined by their subsequent impacts on Li-ion transport kinetics. To understand the transport characteristics of Li and Co ions in bulk LLZO, we performed MLMD simulations for Co-doped cubic LLZO by replacing three Li ions with one Co ion assuming the Co^{3+} oxidation state, i.e. $Li_{7-3x}Co_xLa_3Zr_2O_{12}$, up to $x = 0.5$ with increments of 0.125. Although we did not specifically observe Co ions residing at Zr and La sites in cubic LLZO from the interface simulations within 10 ns, we presume that such defects could be formed at longer time scales and affect Li transport. Co ions at Zr and La sites in cubic LLZO were also considered by replacing one Zr and La ion with one Co ion assuming Co^{4+} and Co^{3+} states (i.e., Li_7Co_x-$La_3Zr_{2-x}O_{12}$ and $Li_7Co_xLa_{3-x}Zr_2O_{12}$), respectively.

For Co substitution at Li sites, no significant volume change is observed (Table S5). The transport characteristics of Li and Co ions in cubic LLZO at 1400 K are shown in Fig. 4 at Co content of $x = 0.5$. Similar to our previous report (with $x = 0.125$) [24], Li and Co ions share the same migration pathways, as evidenced by the Li and Co positional probability density plots presented in the left column of Fig. 4. The occupancy of Co at the Li sites was also verified by site analysis

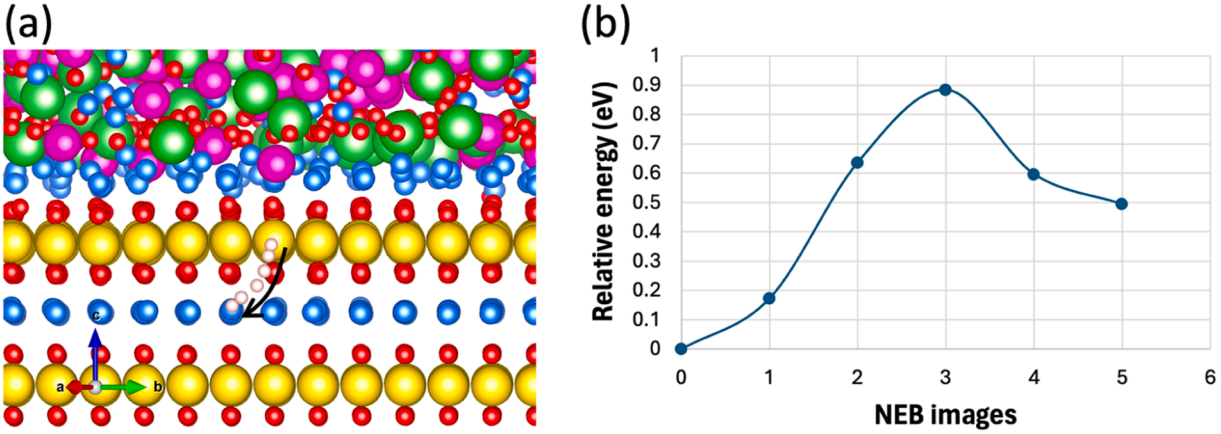

Fig. 3. (a) Hopping path of mobile Li ion (pink) moving from Co vacancy in the outer-most CoO_2 layer to a Li vacancy in the inner Li layer following the arrow direction at the LLZO(001)|LCO(003) interface, obtained by an NEB calculation by MLFF. (b) Corresponding energy pathway indicating 0.88 eV migration barrier for lithiation (arrow direction; NEB images from 0 to 5) and 0.39 eV barrier for delithiation (inversed arrow direction; NEB images from 5 to 0). Note that the curve connecting data points is a guide.

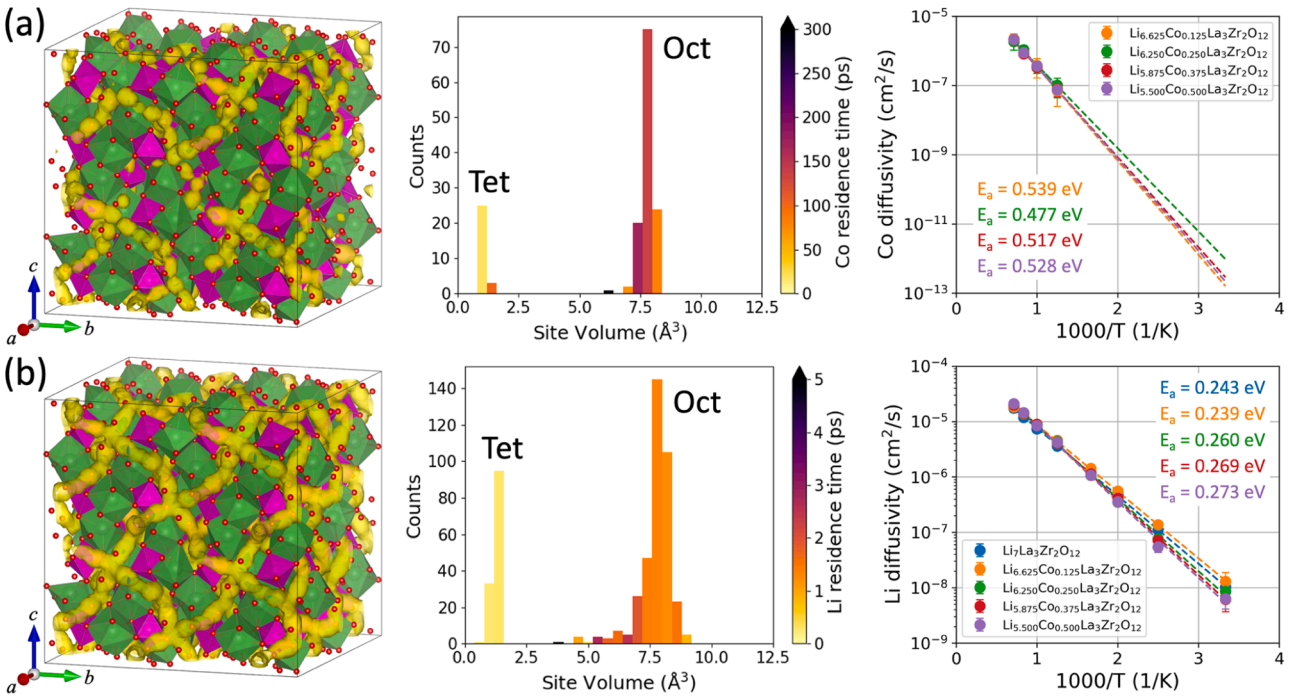

Fig. 4. (Left) positional probability density of ions in a 2 × 2 × 2 cubic LLZO supercell showing diffusion pathways with yellow isosurface (red spheres represent O ions, and green and magenta polyhedra are LaO_8 and ZrO_6, respectively). (Middle) histogram for volume of sites where ions resided in LLZO during MD simulations with a colormap showing the average residence time at each histogram bin (two distinct volume ranges correspond to tetrahedral and octahedral Li sites in LLZO, respectively). (Right) Arrhenius plots for ionic diffusivities for systems with various Co contents (activation energies E_a are also shown with corresponding legend colors) for (a) Co and (b) Li ions. Probability densities and histograms were calculated from MLMD simulations for $[Li_{5.5}Co_{0.5}]La_3Zr_2O_{12}$ at 1400 K, using 100 ps and 1 ns trajectories for Li and Co ions, respectively. In the Arrhenius plots, diffusion data is averaged across 10 MLMD simulations, with error bars representing one standard deviation (see "Simulation Methods with ML potential" section in Supporting Information for simulation details). Diffusivities of Co ions at temperatures ≥ 800 K were used for extrapolation to 300 K.

performed using the *Zeo++* and *Sitator* codes [61,62]. As shown in the middle column of Fig. 4, Co ions predominantly occupy two distinct sites with smaller and larger site volumes, which correspond to the tetrahedral and octahedral Li sites, respectively. The average volumes of the tetrahedral and octahedral sites are 1.25 and 7.75 Å^3, respectively, which are similar to the site volumes in pristine cubic LLZO [63]. This verifies our hypothesis from the interface simulations that Co ions predominantly diffuse into LLZO via Li migration pathways.

Residence time analysis shows that, on average, Li and Co ions occupy the tetrahedral sites for 0.27 and 28.33 ps, respectively—about five times shorter than the octahedral sites (1.41 and 130.51 ps) at 1400 K (middle column in Fig. 4). Co ions reside about 100 times longer than Li at both sites, leading to a disruption of local Li diffusion channels. Nevertheless, the overall effect of Co doping on Li diffusivity appears to be comparatively minor. As shown in the right column of Fig. 4b, the Arrhenius plots of Li transport reveal accompanying marginal increases in the activation energies of Li transport at higher Co doping levels (from 0.243 to 0.273 eV). This result agrees well with previous experiments showing a slight decrease in Li conductivity in Co-incorporated cubic LLZO [24]. This is likely due to the low concentration of Co (at most four Co ions per LLZO unit-cell at the largest content of $x = 0.5$ in a unit cell) compared to all available Li sites that it can occupy, which prevents complete disruption of the overall diffusion network. Moreover, the fact that Co ions tend to reside longer at the octahedral than the tetrahedral sites may prevent complete blocking of Li migration pathways due to the distinct connectivity motifs associated with the two types of sites: an octahedral site connects only two tetrahedral sites, whereas a tetrahedral site links four octahedral sites.

In addition, we performed NEB calculations with DFT to investigate the effect of Co ions on the local energy barriers for Li migration (See "Nudged elastic band calculations" sections and Table S7). Migration barriers are in a range of 0.15 - 0.49 eV without Co, which becomes significantly wider (0 – 2.0 eV) depending on the position of Co ions. It implies that Co ions alter local migration barriers spatiotemporally so that Li ions are activated selectively. Nevertheless, Co ions and their local effects do not considerably affect the "global" activation energy as shown from MD simulations as discussed.

From our MLMD simulations, the Co diffusivity is found to be only one or two orders of magnitude lower than Li diffusivity at temperatures higher than 800 K across a wide range of Co doping levels (right column of Fig. 4a). This indicates relatively fast Co diffusion in cubic LLZO at these high temperatures after interdiffusion across the interfaces, regardless of preexisting Co contents in LLZO. It also explains the wide range of Co distribution observed in LLZO after co-sintering of LLZO/LCO composites at high temperatures [24]. Furthermore, the activation energy of Co diffusion is found about twice larger than that of Li, which leads to about five orders of magnitude lower diffusivity at 300 K by extrapolation. Considering at least 11 times lower concentration of Co than Li at Co content of $x = 0.5$, the conductivity of Co ions at 300 K is expected to be at least six orders of magnitude lower than that of Li ions ($<10^{-10}$ S/cm assuming 10^{-4} S/cm for Li). As a result, we do not expect significant Co diffusion in LLZO at operating conditions.

With Co ions substituted at the Zr site, the lattice parameter decreases linearly with Co concentration up to 0.73 % at the highest doping level of $x = 0.5$ (Table S5). To isolate the effect of cell volume on transport properties, we investigated the transport behavior of Li and Co ions with and without cell volume change. With no change in cell volume, Co doping at the Zr site results in a slight decrease in Li diffusivity, accompanied by a marginal increase in activation energy from 0.243 to 0.267 eV (Fig. 5a). Although this quantitative effect is similar to Co doping at the Li sites (Fig. 4b), Co dopants at Zr sites by contrast do not directly interact with Li. Instead, we hypothesize that it is the local

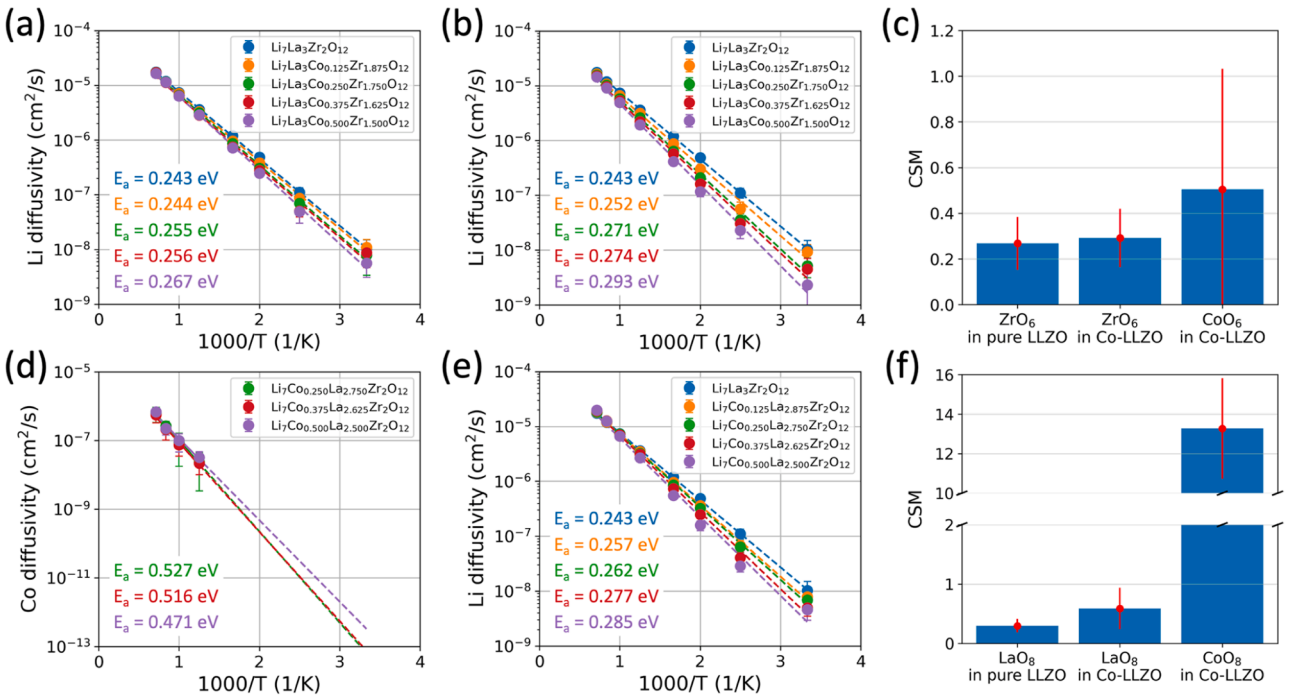

Fig. 5. (a, b) Arrhenius plots for diffusivities of Li ions in cubic LLZO with various Co doping levels at Zr sites (a) with and (b) without the change in cell volume (activation energies E_a are also shown with corresponding legend colors). (c) Histogram of average continuous shape measure (CSM) for the degree of distortion of CoO_6 and ZrO_6 in $Li_{5.5}La_3Co_{0.5}Zr_{1.5}O_{12}$ without a change in cell volume (Co-LLZO), compared to ZrO_6 in pure $Li_7La_3Zr_2O_{12}$ at 300 K (zero CSM represents zero distortion). The red error bar shows one CSM standard deviation. (d, e) Arrhenius plots for ionic diffusivities in cubic LLZO with various Co doping levels at La sites for (d) Co and (e) Li ions. (f) Histogram of average CSM for the degree of distortion of CoO_8 and LaO_8 in $Li_{5.5}Co_{0.5}La_{2.5}Zr_2O_{12}$ (Co-LLZO) and LaO_8 in $Li_7La_3Zr_2O_{12}$ (pure LLZO) at 300K. In the Arrhenius plots, diffusion data is averaged across 10 MLMD simulations, with error bars representing one standard deviation (see "Simulation Methods with ML potential" section in Supporting Information for simulation details). In (d), diffusivities of Co ions at temperatures $\geq$ 800 K were used for extrapolation to 300 K, and the result with $x = 0.125$ Co content is excluded due to poor statistics from too few diffusing Co ions.

structural distortion induced by Co substitution that affects the Li diffusion pathway and the associated kinetics. To verify, we quantified the degree of CoO_6 and ZrO_6 distortions by evaluating the continuous shape measure (CSM) and compared the values to pristine LLZO. Fig. 5c compares the calculated average CSM values of ZrO_6 and CoO_6 in Co-doped LLZO. The results evidence a similar degree of average ZrO_6 distortion in LLZO with and without Co, but the formed CoO_6 moieties are much more distorted than ZrO_6 on average (though with a larger variation). This could contribute to the decreased Li diffusivity shown in Fig. 5a. At reduced cell volumes with higher Co content, a further decrease of Li diffusivity and increase in activation energy are observed (shown in Fig. 5b), which is presumably due to the narrower migration channels that hinder Li ion transport. Overall, our analyses suggest that Co doping at the Zr sites primarily affects Li ion transport kinetics by inducing additional local distortions and reducing the migration channel size.

We would like to note here that we only observed two Co ions escaping from Zr sites to Li sites across a total of 40 MLMD simulations (10 cases at each Co doping level) at 1400 K with decreased cell volume. This may be explained by the energetics of Co doping in cubic LLZO. In particular, the defect formation energy of Co at the Zr site is found to be much lower (0.90 eV at 0 K with the Co^{4+} charge state) compared to that at the Li (1.26 and 1.85 eV for Co^{2+} and Co^{3+}, respectively) and La site ($>$ 2 eV) [64], which is probably related to the preferred six-fold coordination environment of Co with O. At higher temperatures, Co escape from the Zr sites should therefore be rare but possible; however, Li ions should immediately occupy the generated Zr vacancy sites.

In contrast, for Co substituted at the La sites, a number of Co ions moved away from the La sites to the Li sites at 1400 K regardless of Co doping level, consistent with the high formation energy (over 2 eV) predicted at 0K [64]. In fact, when we initially placed Co at the center of the LaO_8 polyhedron and relaxed the model system (Figure S17a), it moved toward the side of the polyhedron, resulting in four-fold coordination with neighboring oxygens (Figure S17b). In addition, no cell volume change was observed with Co doped at the La sites (Table S5). The positional probability density of Co ions, provided in Figure S17c, confirms that the diffusion behavior of Co after escaping from the La sites involves migration along Li pathways, as has also been observed for Co doping at the Li sites. Note that the high formation energy for Co at the La site may be related to the large size mismatch between Co-O and La-O polyhedra. For example, the bond length of Co-O, Zr-O, and La-O within the CoO_6, ZrO_6, and LaO_8 polyhedra are 1.9, 2.1, and 2.6 Å, respectively [65,66].

Fig. 5d presents the Arrhenius plot for Co diffusivity and shows that the estimated diffusivities and activation energies of Co are similar to those for Co doping at the Li sites in cubic LLZO (Fig. 4a). Compared to Co doping at the Li and Zr sites (Figs. 4b and 5a), Co doping at the La site shows stronger impact on Li diffusivity as evidenced in Fig. 5e. We also find that the CSM values of LaO_8 and CoO_8 polyhedra in Co-doped LLZO are much larger than that of LaO_8 in pristine LLZO. In short, we expect the combination of Co diffusion via Li sites and local polyhedral distortions ultimately leads to the decrease in Li diffusivity and increase in activation energy at higher Co doping levels at the La sites.

Overall, our results suggest that Co diffusion in cubic LLZO is fast enough for long-range transport at high temperatures regardless of local Co concentration, enabled by Co sharing well-defined diffusion pathways with Li ions. Our conclusion is consistent with previous experimental observations of Co intrusion into the LLZO separator during high-temperature rapid sintering [24]. Although Co ions may block Li pathways with about 100 times longer residence times at the Li sites compared to Li, the overall effect is only a slight decrease in the average Li diffusion rate. When Co is doped at the La and Zr sites, it also affects Li

diffusivity to some degree due to induced volume change and local structural distortions. This observation again agrees with previous experiment showing slightly decreased Li conductivity in bulk LLZO upon Co interdiffusion from the LLZO|LCO interfaces [24]. Hence, if co-sintering of LLZO and LCO results in a much more significant decrease in Li conductivity in LLZO, we can conclude that it is likely not due to Co ions blocking Li diffusion pathways, but rather other complications such as formation of secondary phases, severe lattice disordering, or transformations from cubic to tetragonal LLZO at GBs and interfaces, accompanied by cation interdiffusion during high-temperature sintering [25].

3.3. Dynamic behavior of Co ions at LLZO GBs

Although it is shown that Co can interdiffuse into the LLZO grain interior via Li channels, it is also possible for Co to move along the GBs of LLZO near the LLZO/LCO interfaces. To investigate the dynamic behavior of Co ions near and at representative GBs of LLZO, a total of six symmetric tilt GB models were generated using three rotation axes of [001], [011], and [111] and two coincident-site lattice (CSL) sigma values for each axis (see "Simulation Methods with ML potential" section in the SI for details of modeling GBs and Table S6 for specifications and calculated GB energies). For each axis, two models with smaller and larger sigma values are chosen to represent less or more disordered GBs as shown in Figure S18. The corresponding GB energies were 0.62, 0.99, and 0.68 J/m^2 for less disordered models and 1.17, 1.23, and 1.26 J/m^2 for more disordered structures with the [001], [011], and [111] rotation axis, respectively. In each GB model, Co ions were initially distributed within grain interior by replacing three Li ions per Co ion, assuming the Co^{3+} oxidation state. In addition, three Co doping levels were considered in each GB model at $x = 0.0625$, 0.125, and 0.25 in $[Li_{7-3x}Co_x]La_3Zr_2O_{12}$ to assess the effects of Co concentration on its dynamic behavior.

Fig. 6a renders a snapshot of $\sum 7(21\bar{3})/[111]$ LLZO GB with Co content of $x = 0.25$ ($Li_{6.25}Co_{0.25}La_3Zr_2O_{12}$) after 10 ns of MLMD simulation, along with the Co distribution profile obtained during the dynamical evolution. At the beginning of the MLMD simulation, Co ions were placed at grain interiors, as shown by the blue line with zero concentration near the GB areas in Fig. 6a. After 10 ns simulation, a noticeable number of Co ions have segregated to the GB regions, as evidenced in the MLMD snapshot and Co density profile. To further investigate Co migration behavior after segregation to the GBs, we calculated the mean-squared displacements (MSDs) of Co located at the GBs versus grain interiors. The results in Fig. 6b show that Co diffusion at GBs is much slower than in grain interiors, which is likely due to more disordered GB structures and less connected Li diffusion pathways [24, 67]. Figure S19 compares Co ion diffusivities at the identified GB structure with different Co contents, in which similar segregation and trapping effects of Co at the GB are observed, even at low Co concentrations. The other GBs with various tilting axes and degrees of disordering (Figures S20-S24) also reveal the same behaviors of Co, highlighting a general phenomenon of Co segregation and trapping at GBs of LLZO regardless of GB composition and misorientation angle [68].

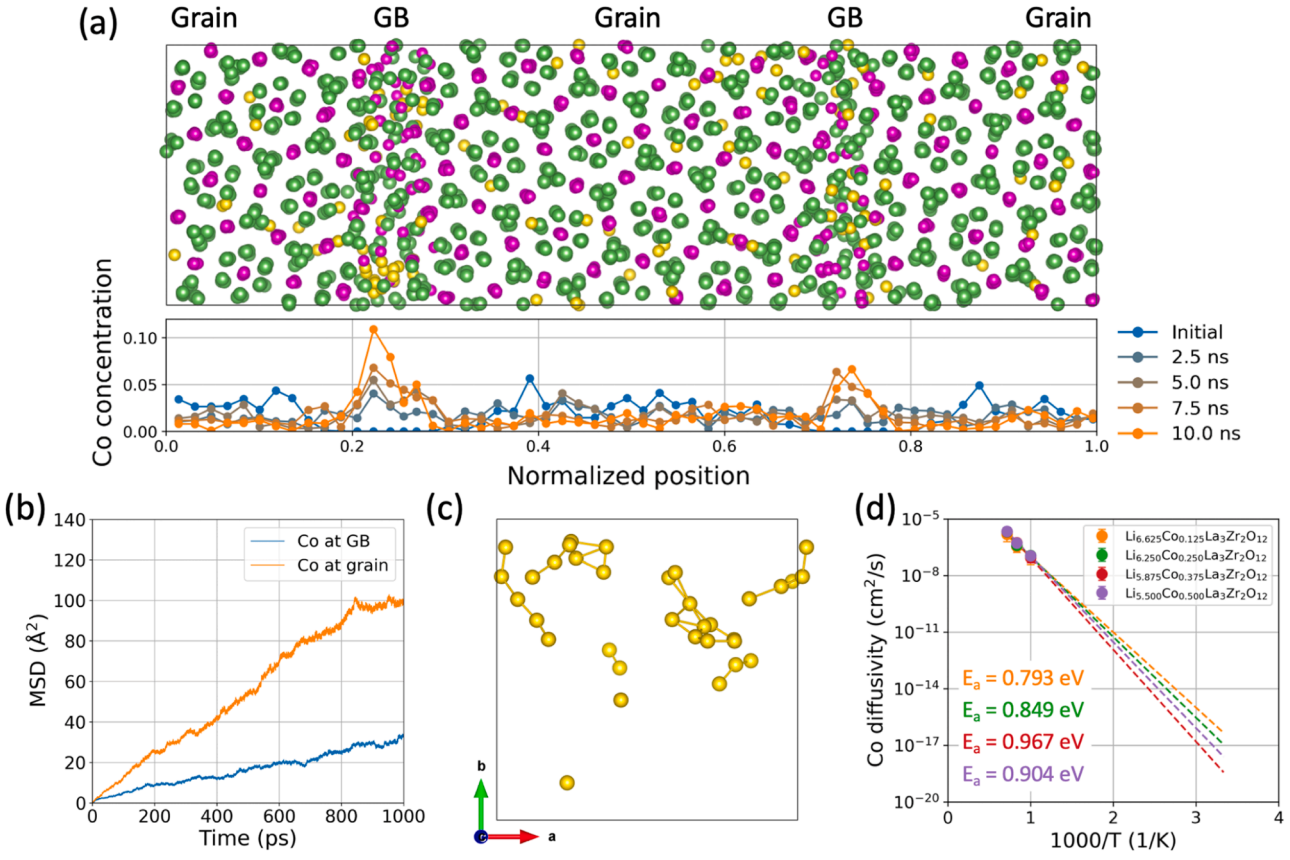

Fig. 6. (a) (Top) atomic structure of $\sum 7(21\bar{3})/[111]$ GB with $x = 0.25$ Co doping level after a 10 ns MLMD simulation at 1300 K, showing Co accumulation at GB regions. (Bottom) distribution profile of Co ions as a function of position normal to GB plane at different simulation times. Yellow spheres represent Co ions, La is green, and Zr is magenta (Li and O ions are not shown for simplicity). (b) Mean squared displacement (MSD) of Co ions at the GB and grain interior at 1300 K over 1 ns simulation time following the prior 10 ns MLMD in (a). (c) Co ions clustering in an amorphous 2 × 2 × 2 LLZO supercell after 11 ns simulation time from an initially uniform distribution. Bonds are drawn for Co ions closer than 3.5 Å (d) Arrhenius plots for Co diffusivities with various Co contents (activation energies E_a are also shown with corresponding legend colors). Diffusivities of Co ions at 1000, 1200, and 1400 K were used for extrapolation to 300 K.

In addition, the results from Fig. 6a and Figures S20-S24 allude to possible Co agglomeration at the GBs of LLZO, which may in turn lead to the formation of Co-rich secondary phases within polycrystalline LLZO [24], or even metallic Co at the LLZO|LCO interface [19]. We hypothesize that the propensity for Co agglomeration is related to the disordered nature of LLZO GBs. To test this hypothesis, we performed additional MLMD simulations of Co-doped amorphous LLZO, which may be considered as a limiting case of complete disorder, and also as a proxy for generic high-angle GB regions [69]. Fig. 6c shows that Co ions that were originally distributed uniformly in amorphous LLZO do indeed agglomerate and form a few number of Co clusters after 11 ns of simulation time. This proves our hypothesis that Co ions form clusters in amorphous LLZO and, by extension, in LLZO GBs with highly disordered atomic geometries. This result also lends additional credence to our previous presumption that the Co clusters at GBs can serve as initial chemical motifs for the formation of Co-rich secondary phases at any LLZO GBs, by reacting with other elements, such as Li and O, as shown in experiments [24,68].

Fig. 6d shows decreased Co diffusivity in amorphous LLZO with increased activation energy at higher Co doping levels. This can be attributed to the trapping effect of forming Co clusters and the sluggish motion of the Co clusters themselves, which is more evident at higher Co doping levels. Extrapolated from Fig. 6d, Co diffusivity in amorphous LLZO ranges from 10^{-18} to 10^{-16} cm^2/s at 300 K over a wide Co stoichiometry range between 0.125 and 0.5, which is about 3 – 6 orders of magnitude lower than that in cubic crystalline LLZO (10^{-13} – 10^{-12} cm^2/s, Fig. 4a). This implies that during operation at room temperature, Co ions are likely to be preferentially trapped at disordered regions in LLZO, including GBs. Nevertheless, Co segregation does not directly affect Li diffusivity in any significant way, as shown in Figure S25. However, Co doping could reduce local Li concentration due to charge balance and indirectly affect Li transport behavior by forming ionically insulating unwanted phases.

4. Conclusion

In conclusion, we developed an ML interatomic potential to investigate the non-equilibrium evolution of complex LLZO|LCO interfaces directly at the atomistic scale. The developed ML model can perform MD simulations with low energy and force errors and predict structural, vibrational, and dynamical properties of LLZO|LCO mixture models as well as bulk LLZO and LCO with similar accuracy to DFT. The model also showed a good predictability for LLZO|LCO mixtures that were not included in the training data, implying its good generalizability for complex local atomic environments at the LLZO|LCO interfaces and reliability to perform accurate atomic simulations.

MLMD simulations for four LLZO|LCO interfaces with various LCO facets as well as LLZO GBs were used to directly probe Co interdiffusion and its consequences for ion dynamics. The results showed that the overall propensity for Co interdiffusion, the preferred cation configuration, and the degree of atomic disorder all depend on the interface chemistry, with Li depletion near the LLZO surface playing a particularly significant determining role. This implies that introducing an additional Li source during co-sintering may alleviate the interfacial degradation.

At high temperatures relevant for processing and across a wide range of Co concentrations, Co ions are predicted to interdiffuse across LLZO|LCO interfaces via interfacial disordering and transport within LLZO grains fast via Li migration channels. Importantly, this does not affect Li transport in LLZO significantly. Near LLZO GBs, Co ions tend to segregate at GBs and become trapped at disordered GB geometries, leading to the formation of Co clusters that can act as prenucleation sites for Co-rich secondary phases at GBs. Because this behavior was not observed to depend on GB tilting axis, the degree of disorder at GB, or the Co concentration, we presume that Co clustering at GBs during processing is a fairly general phenomenon in polycrystalline LLZO.

Overall, our findings elaborate the fundamental relationship between atomic structure, chemistry, and transport behavior at complex LLZO interfaces with the aid of a flexible and accurate ML interatomic potential. Perhaps most importantly, the results suggest practical guidelines for interface design that could minimize interfacial degradation and improve the cycling performance of LLZO-based SSBs.

CRediT authorship contribution statement

Kwangnam Kim: Writing – original draft, Visualization, Validation, Software, Resources, Methodology, Investigation, Formal analysis, Data curation, Conceptualization. **Nicole Adelstein:** Writing – original draft, Formal analysis, Data curation. **Aniruddha Dive:** Data curation. **Andrew Grieder:** Software. **ShinYoung Kang:** Data curation. **Brandon C. Wood:** Writing – review & editing, Supervision, Project administration, Funding acquisition, Conceptualization. **Liwen F. Wan:** Writing – review & editing, Supervision, Project administration, Funding acquisition, Conceptualization.

Declaration of competing interest

The authors declare that they have no known competing financial interests or personal relationships that could have appeared to influence the work reported in this paper.

Acknowledgments

This work was performed under the auspices of the U.S. DOE by the Lawrence Livermore National Laboratory (Contract No DE-AC52–07NA27344) and was sponsored by the Office of Energy Efficiency and Renewable Energy, Vehicle Technologies Office. This work was a part of the U.S.–German collaboration on “Interfaces and Interphases in Rechargeable Li-Metal Based Batteries: Cathode/Solid Electrolyte (CatSE2)” supported by the U.S. Department of Energy (DOE) and the German Federal Ministry of Education and Research (BMBF). An award of computer time was provided by the Innovative and Novel Computational Impact on Theory and Experiment (INCITE) program. This research used resources of the Argonne Leadership Computing Facility, which is a DOE Office of Science User Facility supported under Contract DE-AC02–06CH11357. Additional computational resources were sponsored by the Department of Energy’s Office of Energy Efficiency and Renewable Energy located at the National Renewable Energy Laboratory and the Computing Grand Challenge program from Lawrence Livermore National Laboratory.

Supplementary materials

Supplementary material associated with this article can be found, in the online version, at doi:10.1016/j.ensm.2024.103842.

References

[1] C. Monroe, J. Newman, The impact of elastic deformation on deposition kinetics at lithium/polymer interfaces, J. Electrochem. Soc. 152 (2) (2005) A396.
[2] J.B. Goodenough, Y. Kim, Challenges for rechargeable li batteries, Chem. Mater. 22 (3) (2010) 587–603.
[3] Y.-C. Jung, S.-K. Kim, M.-S. Kim, J.-H. Lee, M.-S. Han, D.-H. Kim, W.-C. Shin, M. Ue, D.-W. Kim, Ceramic separators based on Li+-conducting inorganic electrolyte for high-performance lithium-ion batteries with enhanced safety, J. Power Sources 293 (2015) 675–683.
[4] Y.-S. Hu, Batteries: getting solid, Nature Energy 1 (4) (2016) 16042.
[5] S. Cho, S. Kim, W. Kim, S. Kim, S. Ahn, All-solid-state lithium battery working without an additional separator in a polymeric electrolyte, Polymers (Basel) 10 (12) (2018).
[6] P. Albertus, S. Babinec, S. Litzelman, A. Newman, Status and challenges in enabling the lithium metal electrode for high-energy and low-cost rechargeable batteries, Nature Energy 3 (1) (2018) 16–21.
[7] J.L. Allen, J. Wolfenstine, E. Rangasamy, J. Sakamoto, Effect of substitution (Ta, Al, Ga) on the conductivity of Li7La3Zr2O12, J. Power Sources 206 (2012) 315–319.

[8] Y. Zhu, X. He, Y. Mo, Origin of outstanding stability in the lithium solid electrolyte materials: insights from thermodynamic analyses based on first-principles calculations, ACS Appl. Mater. Interfaces 7 (42) (2015) 23685–23693.

[9] A. Sharafi, E. Kazyak, A.L. Davis, S. Yu, T. Thompson, D.J. Siegel, N.P. Dasgupta, J. Sakamoto, Surface chemistry mechanism of ultra-low interfacial resistance in the solid-state electrolyte Li7La3Zr2O12, Chem. Mater. 29 (18) (2017) 7961–7968.

[10] T. Thompson, S. Yu, L. Williams, R.D. Schmidt, R. Garcia-Mendez, J. Wolfenstine, J.L. Allen, E. Kioupakis, D.J. Siegel, J. Sakamoto, Electrochemical window of the li-ion solid electrolyte Li7La3Zr2O12, ACS Energy Letters 2 (2) (2017) 462–468.

[11] E.J. Cheng, A. Sharafi, J. Sakamoto, Intergranular Li metal propagation through polycrystalline Li6.25Al0.25La3Zr2O12 ceramic electrolyte, Electrochim. Acta 223 (2017) 85–91.

[12] Y. Li, Y. Cao, X. Guo, Influence of lithium oxide additives on densification and ionic conductivity of garnet-type Li6.75La3Zr1.75Ta0.25O12 solid electrolytes, Solid State Ionics 253 (2013) 76–80.

[13] L. Cheng, J.S. Park, H. Hou, V. Zorba, G. Chen, T. Richardson, J. Cabana, R. Russo, M. Doeff, Effect of microstructure and surface impurity segregation on the electrical and electrochemical properties of dense Al-substituted Li7La3Zr2O12, J. Mater. Chem. A 2 (1) (2014) 172–181.

[14] S. Ohta, Y. Kihira, T. Asaoka, Grain boundary analysis of the garnet-like Oxides Li7+X−YLa3−XAXZr2−YNbYO12 (A = Sr or Ca), Frontiers in Energy Research 4 (2016) 30.

[15] A. Banerjee, X. Wang, C. Fang, E.A. Wu, Y.S. Meng, Interfaces and Interphases in All-Solid-State Batteries with Inorganic Solid Electrolytes, Chem. Rev. 120 (14) (2020) 6878–6933.

[16] Y. Ren, T. Danner, A. Moy, M. Finsterbusch, T. Hamann, J. Dippell, T. Fuchs, M. Müller, R. Hoft, A. Weber, L.A. Curtiss, P. Zapol, M. Klenk, A.T. Ngo, P. Barai, B. C. Wood, R. Shi, L.F. Wan, T.W. Heo, M. Engels, J. Nanda, F.H. Richter, A. Latz, V. Srinivasan, J. Janek, J. Sakamoto, E.D. Wachsman, D. Fattakhova-Rohlfing, Oxide-based solid-state batteries: a perspective on composite cathode architecture, Adv. Energy Mater. 13 (1) (2023) 2201939.

[17] G. Bucci, B. Talamini, A. Renuka Balakrishna, Y.-M. Chiang, W.C. Carter, Mechanical instability of electrode-electrolyte interfaces in solid-state batteries, Phys. Rev. Materials 2 (10) (2018) 105407.

[18] P. Barai, T. Rojas, B. Narayanan, A.T. Ngo, L.A. Curtiss, V. Srinivasan, Investigation of delamination-induced performance decay at the Cathode/LLZO interface, Chem. Mater. 33 (14) (2021) 5527–5541.

[19] A.-Y. Hou, C.-Y. Huang, C.-L. Tsai, C.-W. Huang, R. Schierholz, H.-Y. Lo, H. Tempel, H. Kungl, R.-A. Eichel, J.-K. Chang, W.-W. Wu, All-solid-state garnet-based lithium batteries at Work–In Operando TEM investigations of delithiation/lithiation process and capacity degradation mechanism, Adv. Sci. 10 (5) (2023) 2205012.

[20] W.D. Richards, L.J. Miara, Y. Wang, J.C. Kim, G. Ceder, Interface stability in solid-state batteries, Chem. Mater. 28 (1) (2016) 266–273.

[21] Y. Zhu, X. He, Y. Mo, First principles study on electrochemical and chemical stability of solid electrolyte–electrode interfaces in all-solid-state Li-ion batteries, J. Mater. Chem. A 4 (9) (2016) 3253–3266.

[22] Y. Ren, T. Liu, Y. Shen, Y. Lin, C.-W. Nan, Chemical compatibility between garnet-like solid state electrolyte Li6.75La3Zr1.75Ta0.25O12 and major commercial lithium battery cathode materials, J. Materiom. 2 (3) (2016) 256–264.

[23] G. Vardar, W.J. Bowman, Q. Lu, J. Wang, R.J. Chater, A. Aguadero, R. Seibert, J. Terry, A. Hunt, I. Waluyo, D.D. Fong, A. Jarry, E.J. Crumlin, S.L. Hellstrom, Y.-M. Chiang, B. Yildiz, Structure, chemistry, and charge transfer resistance of the interface between $Li7La3Zr_2O_{12}$ Electrolyte and $LiCoO_2$ Cathode, Chem. Mater. 30 (18) (2018) 6259–6276.

[24] W.S. Scheld, K. Kim, C. Schwab, A.C. Moy, S.-K. Jiang, M. Mann, C. Dellen, Y. J. Sohn, S. Lobe, M. Ihrig, M.G. Danner, C.-Y. Chang, S. Uhlenbruck, E. D. Wachsman, B.J. Hwang, J. Sakamoto, L.F. Wan, B.C. Wood, M. Finsterbusch, D. Fattakhova-Rohlfing, The riddle of dark LLZO: cobalt diffusion in garnet separators of solid-state lithium batteries, Adv. Funct. Mater. 33 (43) (2023) 2302939.

[25] M.M.U. Din, L. Ladenstein, J. Ring, D. Knez, S. Smetaczek, M. Kubicek, M. Sadeqi-Moqadam, S. Ganschow, E. Salagre, E.G. Michel, S. Lode, G. Kothleitner, I. Dugulan, J.G. Smith, A. Limbeck, J. Fleig, D.J. Siegel, G.J. Redhammer, D. Rettenwander, A guideline to mitigate interfacial degradation processes in solid-state batteries caused by cross diffusion, Adv. Funct. Mater. n/a (n/a) (2023) 2303680.

[26] M.B. Dixit, A. Verma, W. Zaman, X. Zhong, P. Kenesei, J.S. Park, J. Almer, P. P. Mukherjee, K.B. Hatzell, Synchrotron imaging of pore formation in li metal solid-state batteries aided by machine learning, ACS Applied Energy Materials 3 (10) (2020) 9534–9542.

[27] J. Behler, Four generations of high-dimensional neural network potentials, Chem. Rev. 121 (16) (2021) 10037–10072.

[28] T. Nishiyama, A. Seko, I. Tanaka, Application of machine learning potentials to predict grain boundary properties in fcc elemental metals, Phys. Rev. Materials 4 (12) (2020) 123607.

[29] S. Fujii, A. Seko, Structure and lattice thermal conductivity of grain boundaries in silicon by using machine learning potential and molecular dynamics, Comput. Mater. Sci. 204 (2022) 111137.

[30] T. Yokoi, K. Adachi, S. Iwase, K. Matsunaga, Accurate prediction of grain boundary structures and energetics in CdTe: a machine-learning potential approach, Phys. Chem. Chem. Phys. 24 (3) (2022) 1620–1629.

[31] F.-Z. Dai, B. Wen, H. Xiang, Y. Zhou, Grain boundary strengthening in ZrB2 by segregation of W: atomistic simulations with deep learning potential, J. Eur. Ceram. Soc. 40 (15) (2020) 5029–5036.

[32] K. Kim, A. Dive, A. Grieder, N. Adelstein, S. Kang, L.F. Wan, B.C. Wood, Flexible machine-learning interatomic potential for simulating structural disordering behavior of Li7La3Zr2O12 solid electrolytes, J. Chem. Phys. 156 (22) (2022) 221101.

[33] N. Artrith, A.M. Kolpak, Understanding the composition and activity of electrocatalytic nanoalloys in aqueous solvents: a combination of DFT and accurate neural network potentials, Nano Lett. 14 (5) (2014) 2670–2676.

[34] S.K. Natarajan, J. Behler, Neural network molecular dynamics simulations of solid–liquid interfaces: water at low-index copper surfaces, Phys. Chem. Chem. Phys. 18 (41) (2016) 28704–28725.

[35] V. Quaranta, M. Hellström, J. Behler, Proton-transfer mechanisms at the Water–ZnO Interface: the role of presolvation, J. Phys. Chem. Lett. 8 (7) (2017) 1476–1483.

[36] M.F. Calegari Andrade, H.-Y. Ko, L. Zhang, R. Car, A. Selloni, Free energy of proton transfer at the water–TiO2 interface from ab initio deep potential molecular dynamics, Chem. Sci. 11 (9) (2020) 2335–2341.

[37] S. Lorenz, A. Groß, M. Scheffler, Representing high-dimensional potential-energy surfaces for reactions at surfaces by neural networks, Chem. Phys. Lett. 395 (4) (2004) 210–215.

[38] X. Shen, J. Chen, Z. Zhang, K. Shao, D.H. Zhang, Methane dissociation on Ni(111): a fifteen-dimensional potential energy surface using neural network method, J. Chem. Phys. 143 (14) (2015) 144701.

[39] B. Kolb, X. Luo, X. Zhou, B. Jiang, H. Guo, High-dimensional atomistic neural network potentials for molecule–surface interactions: hCl scattering from Au(111), J. Phys. Chem. Lett. 8 (3) (2017) 666–672.

[40] N. Artrith, B. Hiller, J. Behler, Neural network potentials for metals and oxides – First applications to copper clusters at zinc oxide, Physica Status Solidi (b) 250 (6) (2013) 1191–1203.

[41] E.L. Kolsbjerg, A.A. Peterson, B. Hammer, Neural-network-enhanced evolutionary algorithm applied to supported metal nanoparticles, Phys. Rev. B 97 (19) (2018) 195424.

[42] N. Artrith, Machine learning for the modeling of interfaces in energy storage and conversion materials, Journal of Physics: Energy 1 (3) (2019) 032002.

[43] Y. Shao, L. Knijff, F.M. Dietrich, K. Hermansson, C. Zhang, Modelling bulk electrolytes and electrolyte interfaces with atomistic machine learning, Batteries & Supercaps 4 (4) (2021) 585–595.

[44] W. Jeong, D. Yoo, K. Lee, J. Jung, S. Han, Efficient atomic-resolution uncertainty estimation for neural network potentials using a replica ensemble, J. Phys. Chem. Lett. 11 (15) (2020) 6090–6096.

[45] J. Wang, A.A. Panchal, G. Sai Gautam, P. Canepa, The resistive nature of decomposing interfaces of solid electrolytes with alkali metal electrodes, J. Mater. Chem. A 10 (37) (2022) 19732–19742.

[46] M.L. Holekevi Chandrappa, J. Qi, C. Chen, S. Banerjee, S.P. Ong, Thermodynamics and kinetics of the cathode–electrolyte interface in all-solid-state Li–S batteries, J. Am. Chem. Soc. 144 (39) (2022) 18009–18022.

[47] V.L. Deringer, Modelling and understanding battery materials with machine-learning-driven atomistic simulations, J. Phys.: Energy 2 (4) (2020) 041003.

[48] T.T. Vu, H.J. Cheon, S.Y. Shin, G. Jeong, E. Wi, M. Chang, Hybrid electrolytes for solid-state lithium batteries: challenges, progress, and prospects, Energy Storage Materials 61 (2023) 102876.

[49] P.V.F. de Blasio, P.B. Jorgensen, J.M. Garcia Lastra, A. Bhowmik, Nanosecond MD of battery cathode materials with electron density description, Energy Storage Materials 63 (2023) 103023.

[50] Y. Zhang, H. Huang, J. Tian, C. Li, Y. Jiang, Z. Fan, L. Pan, Modelling electrified microporous carbon/electrolyte electrochemical interface and unraveling charge storage mechanism by machine learning accelerated molecular dynamics, Energy Storage Mater. 63 (2023) 103069.

[51] A. Singraber, T. Morawietz, J. Behler, C. Dellago, Parallel multistream training of high-dimensional neural network potentials, J. Chem. Theory Comput. 15 (5) (2019) 3075–3092.

[52] A. Singraber, J. Behler, C. Dellago, Library-based LAMMPS implementation of high-dimensional neural network potentials, J. Chem. Theory Comput. 15 (3) (2019) 1827–1840.

[53] J. Behler, M. Parrinello, Generalized neural-network representation of high-dimensional potential-energy surfaces, Phys. Rev. Lett. 98 (14) (2007) 146401.

[54] A. Pankratz, Forecasting With Dynamic Regression Models, John Wiley & Sons, New York, 1991.

[55] D.-J. Liu, J.W. Evans, Fluorine spillover for ceria- vs silica-supported palladium nanoparticles: a MD study using machine learning potentials, J. Chem. Phys. 159 (2) (2023) 024101.

[56] G. Larraz, A. Orera, M.L. Sanjuán, Cubic phases of garnet-type Li7La3Zr2O12: the role of hydration, J. Mater. Chem. A 1 (37) (2013) 11419–11428.

[57] D. Kramer, G. Ceder, Tailoring the morphology of LiCoO2: a first principles study, Chem. Mater. 21 (16) (2009) 3799–3809.

[58] E. Rangasamy, J. Wolfenstine, J. Sakamoto, The role of Al and Li concentration on the formation of cubic garnet solid electrolyte of nominal composition Li7La3Zr2O12, Solid State Ionics 206 (2012) 28–32.

[59] G. Henkelman, H. Jónsson, Improved tangent estimate in the nudged elastic band method for finding minimum energy paths and saddle points, J. Chem. Phys. 113 (22) (2000) 9978–9985.

[60] M. Okubo, Y. Tanaka, H. Zhou, T. Kudo, I. Honma, Determination of activation energy for Li Ion diffusion in electrodes, J. Phys. Chem. B 113 (9) (2009) 2840–2847.

[61] T.F. Willems, C.H. Rycroft, M. Kazi, J.C. Meza, M. Haranczyk, Algorithms and tools for high-throughput geometry-based analysis of crystalline porous materials, Microporous Mesoporous Mater. 149 (1) (2012) 134–141.

[62] L. Kahle, A. Musaelian, N. Marzari, B. Kozinsky, Unsupervised landmark analysis for jump detection in molecular dynamics simulations, Phys. Rev. Materials 3 (5) (2019) 055404.
[63] A.e.a. Grieder, The effect of interatomic potentials on non-equilibrium structure and ionic diffusivity, Submitted (2023).
[64] L.J. Miara, W.D. Richards, Y.E. Wang, G. Ceder, First-principles studies on cation dopants and Electrolyte|Cathode interphases for lithium garnets, Chem. Mater. 27 (11) (2015) 4040–4047.
[65] H. Xie, J.A. Alonso, Y. Li, M.T. Fernández-Díaz, J.B. Goodenough, Lithium distribution in aluminum-free cubic Li7La3Zr2O12, Chem. Mater. 23 (16) (2011) 3587–3589.
[66] K. Kataoka, J. Akimoto, Single-crystal growth, crystal structure analysis and physical properties of lithium overstoichiometric Li1+xCoO2, Solid State Ionics 262 (2014) 106–109.
[67] D.J. Kalita, S.H. Lee, K.S. Lee, D.H. Ko, Y.S. Yoon, Ionic conductivity properties of amorphous Li–La–Zr–O solid electrolyte for thin film batteries, Solid State Ionics 229 (2012) 14–19.
[68] X. Liu, R. Garcia-Mendez, A.R. Lupini, Y. Cheng, Z.D. Hood, F. Han, A. Sharafi, J. C. Idrobo, N.J. Dudney, C. Wang, C. Ma, J. Sakamoto, M. Chi, Local electronic structure variation resulting in Li 'filament' formation within solid electrolytes, Nat. Mater. 20 (11) (2021) 1485–1490.
[69] T.W. Heo, A. Grieder, B. Wang, M. Wood, T. Hsu, S.A. Akhade, L.F. Wan, L.-Q. Chen, N. Adelstein, B.C. Wood, Microstructural impacts on ionic conductivity of oxide solid electrolytes from a combined atomistic-mesoscale approach, Npj Comput. Mater. 7 (1) (2021) 214.